THE JOURNAL OF PHYSICAL CHEMISTRY B
A JOURNAL OF THE AMERICAN CHEMICAL SOCIETY

pubs.acs.org/JPCB

Article

Insights into the Dual Shuttle Catalytic Mechanism of Guanine Deaminase

Asmita Sen, Vandana Gaded, Prabha Jayapal, Gopalan Rajaraman,* and Ruchi Anand*

Cite This: *J. Phys. Chem. B* 2021, 125, 8814–8826

Read Online

ABSTRACT: Guanine deaminases (GD) are essential enzymes that help in regulating the nucleobase pool. Since the deamination reaction can result in the accumulation of mutagenic bases that can lead to genomic instability, these enzymes are tightly regulated and are nonpromiscuous. Here, we delineate the basis of their substrate fidelity via entailing the reaction mechanism of deamination by employing density functional theory (DFT) calculations on NE0047, a GD from *Nitrosomonas europaea*. The results show that, unlike pyrimidine deaminases, which require a single glutamic acid as a proton shuttle, GDs involve two amino acids, E79 and E143 (numbering in NE0047), which control its reactivity. The hybrid quantum mechanics/molecular mechanics (QM/MM) calculations have shown that the first Zn-bound proton transfer to the N3 atom of the substrate is mediated by the E79 residue, and the second proton is transferred to the amine nitrogen of substrate via E143. Moreover, cluster models reveal that the crystallographic water molecules near the active site control the reactivity. A comparison with human GD reveals that the proposed catalytic mechanism is generic, and the knowledge generated here can be effectively applied to design selective inhibitors.

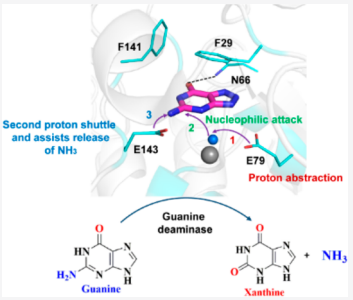

INTRODUCTION

Though living cells are capable of synthesizing biomolecules via de novo biosynthetic pathways, it takes enormous amounts of energy inputs.[1] In order to circumvent the high-energy demand, cells have devised salvage and catabolic pathways to recover and reshuffle the nucleobases obtained from the diet or via nucleic acid degradation.[2,3] To facilitate the shuffling, nucleobase deaminases serve as central players in these pathways and maintain a stringent control on the total purine and pyrimidine nucleotide pool, the prime building blocks of the genetic material, DNA and RNA.[4−6] However, deamination of nucleobases results in mutagenic bases like xanthine, hypoxanthine, oxaine, etc. and can lead to aberrations in the coding of DNA. As a result, a high degree of control on the concentration as well as the activity of these deaminases is maintained.[7,8] Further, to prevent accidental incorporation of the aberrant bases, repair enzymes such as endonuclease V and endonuclease VIII that remove these mutagens as part of the repair machinery also monitor the genetic status.[8] Studies on these nucleobase deaminases have demonstrated that an interplay between the substrate and the stereoenergetics of the active site is at play for the reaction to be successful.[9−11] Of the various enzymes that partake in the nucleotide metabolism, guanine deaminases (GD) are one of the key enzymes that catalyze the conversion of guanine to xanthine.[6,10,12] The GD reaction results in the removal of the guanine base from the nucleobase pool and in turn affects the cellular GTP and the guanylate nucleotide level that directly impacts the rate of DNA synthesis in the cell.[12−14] Since GDs play such an essential role in maintaining the integrity of the cell, it is paramount to understand the reaction mechanism that enables it to select only the cognate substrate. For instance, recent work has shown that GDs only accept guanine as a substrate and do not catalyze any other base such as adenine; even bases with minimal substitutions on the guanine scaffold such as 9-methylguanine, 1-methylguanine, etc. are rejected.[9,10] Oddly enough, despite their stringency for their cognate substrates, GDs catalyze the deamination of the triazine, ammeline, a mystery that the mechanistic insights will help in detangling. Another distinct feature of the nucleobase deaminases is that the prokaryotic and eukaryotic enzymes harbor entirely different folds. While prokaryotes adopt the $\alpha\beta\alpha$ layered cytidine deaminase fold and only involve zinc as the metal for effective deamination[6,10] (Figure 1A−C), the eukaryotic GDs harbor a triosephosphate isomerase fold and can accept a variety of metals to assist the reaction.[15] Since GDs are essential enzymes, these structural differences between the human and pathogenic GDs, along with the mechanistic nuances, can be exploited toward drug design to assist in selective targeting of bacterial GDs.

The catalytic mechanism of nucleobase deaminases, especially pyrimidine yeast cytosine deaminase (yCD), has been widely studied.[5,16−18] It has been established that, in yCD, a single

Received: July 9, 2021
Revised: July 19, 2021
Published: July 29, 2021

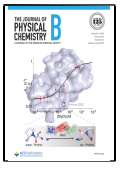

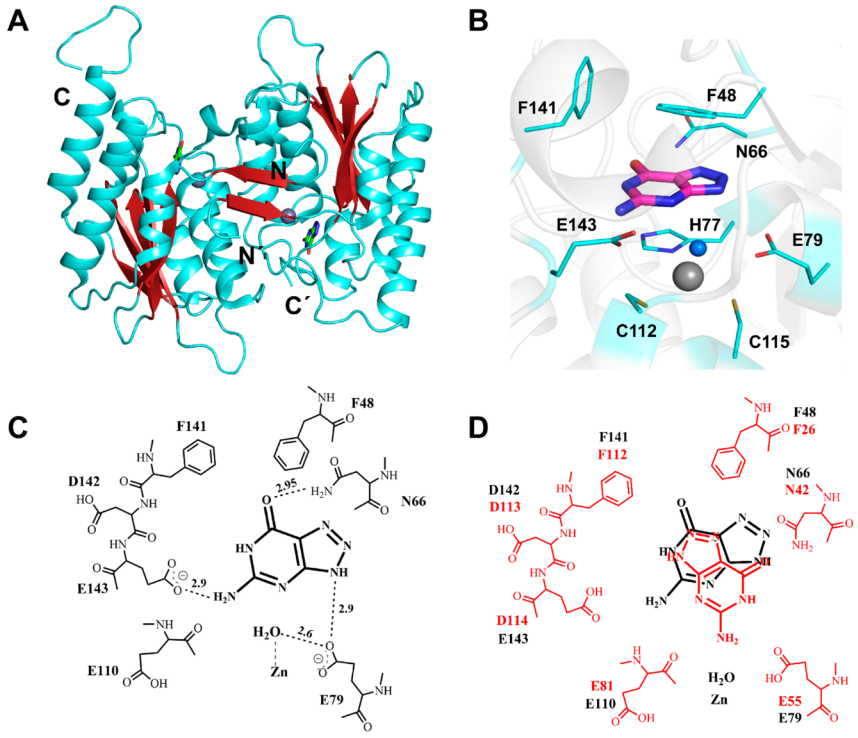

Figure 1. Structural overview of GD: (A) homodimeric structure of NE0047, (B, C) active-site network of NE0047 in complex with 8-azaguanine, and (D) 8-azaguanine modeled in a crystallographic position of the imidazole-bound structure of *B. subtilis* GD (bGD). Residues in red belong to bGD, and those in black belong to NE0047.

glutamic acid residue is responsible for the proton shuttle that assists the zinc-bound water molecule for nucleophilic attack on the C4 carbon of cytosine.[16,19] In the case of GDs, initial reports by Yao and co-workers have attempted to delineate the mechanism via ONIOM calculations.[20] However, the lack of enzyme−substrate crystal structures of GDs at that time has led to inconclusive results (Figure 1D). Therefore, to understand the nuances of the reaction mechanism and to establish the importance of the active-site residues that partake in the reaction, this study was undertaken. Keeping the above facts in mind, in the present study, we have focused on the purine base guanine and the triazine ammeline to study the GD-catalyzed deamination. The crystal structures of GD complexed with 8-azaguanine and ammeline are already known (PDB entry 4HRQ and 4LCO, respectively), and these high-resolution crystal structures provided us with a good starting structure for our computational study.[9,10] Herein, we have performed a classical molecular dynamics simulation followed by a series of two-layered ONIOM calculations (quantum mechanics/molecular mechanics, QM/MM) on the guanine-bound GD to thoroughly assess the important configurational properties of the system during the reaction and to understand the mechanistic details at a molecular level. Moreover, we extended the findings of the ONIOM results to quantum mechanical (QM) calculations on three types of active-site model systems of ammeline-bound GD. This was done to decipher the effect of residues from the secondary coordination sphere on the reaction rate and propose a quantum mechanical model to study the reaction mechanism of these complex systems. The energetics of the guanine versus ammeline deamination has also been investigated, and implications toward the evolution of the enzyme mechanism have been discussed.

METHODOLOGY

Molecular Dynamic Simulations. The molecular dynamics simulations have been carried out using the GROMACS 2020 software.[21] The molecular topology file of the metal-containing nonstandard active site was prepared using the Antechamber Python parser interface (ACPYPE) script and AmberTools.[22]

We have taken the initial coordinates from the X-ray crystallographic structure of NE0047 complexed with 8-azagaunine (PDB entry 4HRQ; resolution: 1.9 Å) and replaced the 8-azagaunine substrate with guanine using the PyMOL 2.4.1 version.[23] The coordinates of guanine have been obtained after the geometry optimization with the B3LYP as functional[24] and 6-31G* basis set using the Gaussian 09 suite of programs.[25] The final model contains the Zn-bound metalloenzyme, guanine, and crystallographic waters. Next, protonation states of the residues have been assigned using the H++ server at pH 7.0 and at the dielectric constant of 4.0.[26] The resulting protein−ligand system is then placed in a $75 \times 75 \times 75$ Å^3 cubic box of the TIP3P water model.[27] Further, 10 mmol of the sodium chloride salt is added to the system as well as 8 additional sodium ions to neutralize the entire system.

The system was then minimized following 1000 steps of the steepest descent to optimize the potential energy of the system and to remove the bad contacts and steric clashes.[28] The system is then slowly heated from 0.1 K to close to 300−310 K over 1 ns at a constant volume and temperature (*NVT*) ensemble using a V-rescale thermostat[29] where we have employed weak harmonic constraints (force constant = 25.0 kcal mol^{-1} A^{-2}) on the solute to avoid any void formation inside the solvate box. The heating procedure is further followed by a slow removal of constraints in 8 stages of equilibration (with restraints of 25, 20, 15, 11, 6, 4, 2, 1 kcal mol^{-1} A^{-2}) over 500 ps of each. Each equilibration is

https://doi.org/10.1021/acs.jpcb.1c06127
J. Phys. Chem. B 2021, 125, 8814−8826

followed by 1000 steepest descent energy minimization, and the minimized structure has been employed as the starting structure for the next equilibration. After the 8 stages of equilibration, an unrestrained equilibration was run for 5 ns in an isothermal−isobaric (*NPT*) ensemble to reach a steady pressure of 1 atm. The temperature is maintained to 300 K using a V-rescale thermostat, and the pressure is kept fixed at 1 atm using a Parrinello−Rahman barostat[30] with a pressure relaxation time of 0.1 ps. This equilibration procedure is sufficient to converge the properties of the system, like pressure and temperature. Finally, 15 ns of unrestrained dynamics was performed using the Nose−Hoover thermostat[31] at 300 K with a 0.6 ps coupling constant. During the simulation, all bonds were constrained using the LINCS algorithm.[32] The entire production run has been carried out with a time step of 2 fs, and the coordinates were saved in an interval of 1 ps. The spherical cutoff distance for all nonbonded interactions (electrostatic and van der Waals interactions) is set to 10 Å. The particle mesh Ewald (PME) method has been used to calculate the long-range electrostatic interactions using a cubic interpolation of order 4.[33] Periodic boundary conditions in all three directions have been used, and the SHAKE algorithm[34] has been used to restrain the equilibrium bond distances of the TIP3P water molecules.

The estimated average root-mean-square deviation (RMSD) of the protein backbone is 0.12 Å, while the RMSD value for the ligand (guanine) is estimated to be 0.11 Å (Figure S1A) during the last 5 ns of the production run. The significantly low RMSD value indicates that the system has equilibrated enough for further study. The average binding energy of the guanine ligand to the protein is −182 kJ/mol, indicating the stability of the ligand inside the protein. Therefore, the 15 ns of the final production run is sufficient for the cluster analysis and ONIOM calculations in the following steps.

ONIOM Calculations. For the quantum mechanics/molecular mechanics calculations, we have extracted the most populated representative snapshot by the clustering analysis of the overall MD trajectories. Herein, a statistically more precise method has been employed than stochastically taking snapshots within a particular time scale. For the QM/MM setup, we have considered all of the amino acid residues within 10 Å of the Zn-bound guanine, including Phe48, Asn66, Val68, Ala75, Ala76, His77, Ala78, Glu79, Ile80, Thr107, Ala109, E110, Pro111, Cys112, Val113, Met114, Cys115, Phe116, G117, Ala118, Val119, Phe141, Asp142, Glu143, Gly144, Pro145, Arg146, Pro147 residues, and the water molecules which are in the close vicinity of the active site. The average binding energy exerted by the residues present within the 10 Å cavity around the ligand is −198 kJ/mol, which is slightly higher than the binding energy calculated in the presence of the entire protein (−182 kJ/mol). The binding energy of the ligand inside a cavity is composed of several interactions including stabilizing and destabilizing interactions. Therefore, it is a direct measure of the stability of the ligand inside the binding site and can give a quantitative idea of the stabilizing and destabilizing interactions by the surrounding residues on the ligand. This suggests that the residues beyond 10 Å are unlikely to affect the ligand binding as well as the associated reaction mechanism, and the aforementioned 27 residues within the 10 Å cavity are sufficient for our further study. A similar study by Yan and co-workers on the deamination reaction of *Bacillus subtilis* guanine deaminase (bGD) revealed that all secondary coordination sphere residues in the ligand-binding pocket are sufficient for the ONIOM calculations, explaining the guanine deamination satisfactorily.[20]

The final QM/MM setup contains a total of 411 atoms. A two-layer ONIOM (QM: MM) method implemented in Gaussian 09 software is used for the QM/MM calculations.[35,36] The entire system under consideration has been divided into two layers: the high layer, which is treated with a density functional method, and the low layer, which is treated with a lower level of theory. The QM region is defined by the first-coordination-sphere residues of Zn in the active site, containing one histidine (H77), two cysteines (C112 and C115), one crystallographic water molecule, guanine as substrate, and two glutamic acid residues (E143 and E79) in the secondary coordination sphere. The remaining system was treated as the MM region. Histidine is modeled as methylimidazole, C112 and C115 as SCH_3, and glutamic acid residues (E143 and E79) as CH_3COO^-. The QM/MM electrostatic interactions have been treated in a classical way by using an electrical embedding scheme for geometry optimization as well as for frequency calculations. Fixed atomic point charges have been used in the core and the environment.[37,38]

During the geometry optimization, the entire system has been divided into two segments, active and static. The active region includes the QM subregion and an active MM region, which is defined by Ala75, Ala76, Ala78, and Ile80. The remaining MM part is considered as the static region, which was frozen during optimizations, only influencing the active region through the electrostatic effect of the point charges. The QM region is treated by the density functional theory (DFT) method using hybrid dispersion-corrected B3LYP-D2 as the functional[39,40] along with the LACVP basis set, which comprises a double-ζ quality basis set with the Los Alamos effective core potential, LanL2DZ for Zn metal, and a 6-31G* basis set[41−43] for the nonmetals (C, H, N, O, and S) present in the system. The above protocol has been employed for geometry optimization as well as for frequency calculations. The dispersion-corrected B3LYP functional has proven to be useful to account for the weak interactions (hydrophobic and hydrogen-bonding interactions) between the enzyme and the substrate molecule.[41−43] The geometries of all stationary points, including reactants, intermediates, and the transition states, are fully optimized. Transition states were located in the following way: first, a stepwise relaxed potential energy surface scan was performed varying the reaction coordinates such as the interatomic distances or valence angles between the atoms involving in the bond-breaking and -making process. Second, a molecular Hessian associated with the highest-energy point in the calculated scan profile was used for the subsequent complete geometry optimization of the transition states. Harmonic vibrational frequency analysis has been performed to characterize all the stationary points in the potential energy surface at the temperature of 298.15 K and to evaluate the zero-point energy corrections. All transition states were characterized by a single negative frequency. At the same time, the intermediates are characterized by all positive frequencies. The ONIOM energies were further modified by the single-point energy calculations using an all-electron larger basis set Def2-TZVP for all atoms following the ONIOM (B3LYP/Def2-TZVP: AMBER) method. The final quoted energies were dispersion-corrected ONIOM-EE energies, including zero-point energy corrections obtained from the frequency calculations

$$E_{\mathrm{ONIOM(QM:MM)}} = E_{\mathrm{QM,model}} + E_{\mathrm{MM,real}} - E_{\mathrm{MM,model}} + E_{\mathrm{disp}} + \mathrm{ZPE}_{\mathrm{corr}}$$

https://doi.org/10.1021/acs.jpcb.1c06127
J. Phys. Chem. B 2021, 125, 8814−8826

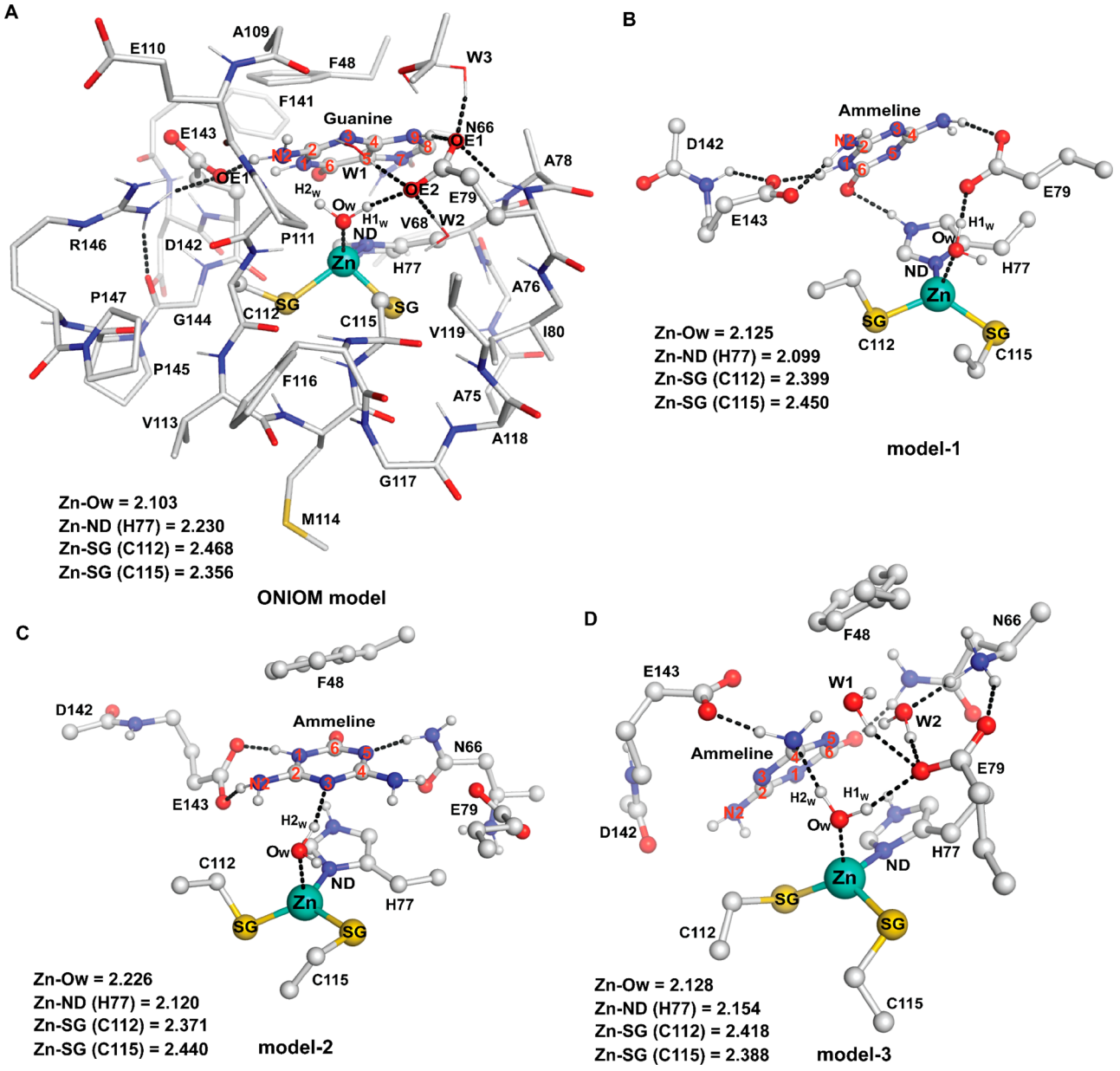

Figure 2. (A) ONIOM (B3LYP-D2/[LanL2DZ(Zn);6-31G*(others): AMBER) optimized structure of guanine-bound GD (r) complex and B3LYP-D3/[Lanl2DZ(Zn);6-31G*(others) optimized structures of (B) model-1, (C) model-2, and (D) model-3 of ammeline-bound GD (r_a) complex. Bond distances are depicted in Ångström (Å) units. Zinc, sulfur, oxygen, nitrogen, carbon, and hydrogen atoms are expressed as green, yellow, red, blue, gray, and white spheres.

DFT Calculations. All of the QM-only DFT calculations were carried out using the Gaussian 09 suite of program.[44−46] An unrestricted hybrid dispersion-corrected B3LYP-D3 functional[44−46] has been used for all the gas-phase optimizations as well as frequency calculations. The same protocol mentioned in the ONIOM calculation section has been used for the geometry optimizations and frequency calculations for the QM-only studies. Similarly, the refinement of the gas-phase energies of the stationary points has been performed by the single-point energy calculations using the def2TZVP basis set for all atoms in the same level of theory. Single-point energy calculations were performed to consider the effect of protein environment on the optimized gas-phase geometries using the conductor-like polarizable continuum model (CPCM) employing the B3LYP-D3 level of theory.[47] The CPCM calculations used UFF atomic radii and the defaulted water solvent parameters. The dielectric constant has been fixed at the standard value of $\varepsilon = 4$ to consider the combined effect of the protein and water medium in the surroundings.[48] The final quoted DFT energies were B3LYP-D3 solvation energies, including zero-point energy corrections obtained from the frequency calculations. Energy decomposition analysis (EDA) has been used to elucidate the various contributing factors which are playing an important role in dictating the stability of the intermediates and transition states involved (Figure S1B). The electronic interaction energy, ΔE_{int}, between two fragments is composed of three energy terms, namely, (i) the electrostatic interaction energy, $\Delta E_{elstat,}$ (ii) the repulsive exchange interaction energy, ΔE_{Pauli}, and (iii) the orbital interaction ΔE_{orb}, $\Delta E_{int} = \Delta E_{elstat} + \Delta E_{Pauli} + \Delta E_{orb.}$ The first two repulsive types of energy contributions (ΔE_{elstat} and ΔE_{Pauli}) can be combined into a single term, ΔE_{steric}. Therefore, $\Delta E_{int} = \Delta E_{steric} + \Delta E_{orb}$. ΔE_{steric} is responsible for destabilization,

https://doi.org/10.1021/acs.jpcb.1c06127
J. Phys. Chem. B 2021, 125, 8814−8826

Scheme 1. Reaction Mechanism Proposed for the Deamination of Guanine by GD[a]

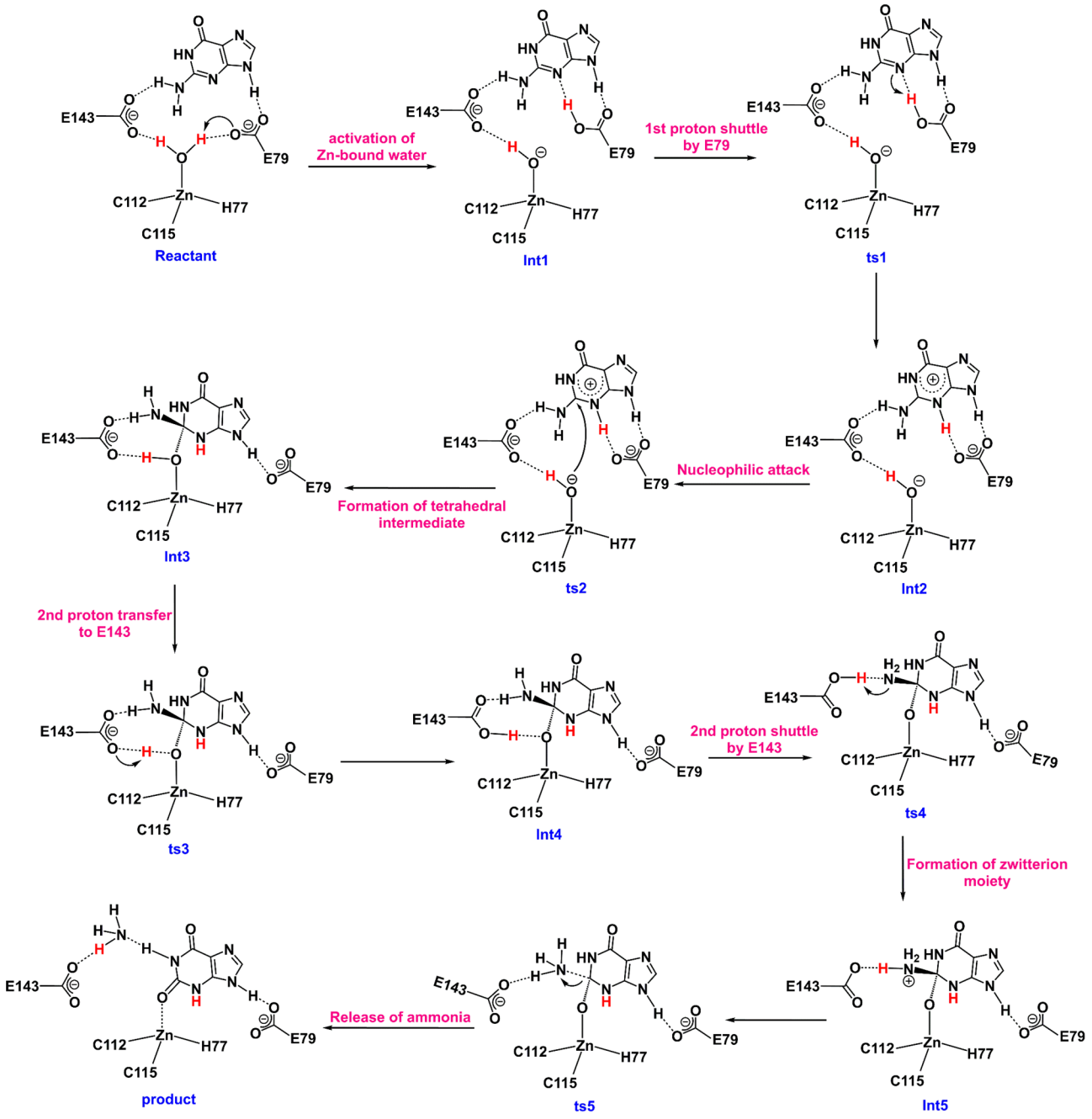

[a]Hydrogen atoms of zinc-bound water are shown in red.

and ΔE_{orb} is responsible for destabilization, and ΔE_{orb} contributes to energy stabilization.

The natural charges of all species were calculated using the natural bonding orbital (NBO) approach implemented in the Gaussian 09 package. All figures were generated using the PyMOL 2.4.1 version.[29] We have used notations for easy understanding of the various species, for instance, $[species]_{a(x)}$, where a stands for ammeline while the number in the parentheses denotes the model.

RESULTS AND DISCUSSION

The structure and the substrate specificity of NE0047 from *Nitrosomonas europaea*, a Gram-negative chemolithoautotroph bacteria (PDB entry 2G84) as a nucleobase deaminase, have been investigated previously by Anand and co-workers.[9,10] A series of purine and pyrimidine bases and their analogues have been explored for the enzymatic deamination reactions, and it was found that, among all the nucleobases, NE0047 can selectively catalyze the C2 deamination of guanine. It exhibited a catalytic efficiency, ∼50% of guanine, for the structurally divergent triazine ammeline. Here, using GD-bound 8-azaguanine as starting points, we have performed ONIOM calculations. We shed light on the mechanistic details and the various contributing factors that dictate the rate of the deamination reaction.

Active-Site Architecture upon Guanine Binding. The active site of dimeric NE0047 from *Nitrosomonas europaea*

https://doi.org/10.1021/acs.jpcb.1c06127
J. Phys. Chem. B 2021, 125, 8814−8826

enzyme contains a zinc metal coordinated to H77, C112, C115, and a crystallographic water molecule (W703) in a tetrahedral fashion. The Zn−ND, Zn−SG(C112), Zn−SG(C115), and Zn−O_w bond distances in the native GD are 2.048, 2.328, 2.260, and 2.053 Å, respectively, while the respective SG(C112)−Zn−SG(C115), SG(C112)−Zn−O_w, SG(C115)−Zn−O_w, SG(C112)−Zn−ND(H77), SG(C115)−Zn−ND(H77), and O_w−Zn−ND(H77) angles are found to be 117.85°, 104.01°, 106.94°, 105.70°, 111.16°, and 110.93°.[9,10] The tetrahedral environment around the Zn metal in the active site in GD has been maintained upon guanine binding and can be reproduced by the ONIOM calculations. The ONIOM computed respective bond distances are found to be 2.230, 2.468, 2.356, and 2.103 Å (Figure 2A), which are in excellent agreement with those measured in the high-resolution crystal structure (2.133, 2.368, 2.400, 2.370 Å, respectively, Table S1). In the ligand-binding cavity, the substrate is anchored near the Zn-binding site by the hydrogen-bonding interactions between the amine group ($-NH_2$) and the N9−H of guanine with the OE1 of E143 (1.694 Å) and E79 (1.604 Å), respectively (Figure 2A). Moreover, the purine ring of the substrate is further stabilized by the hydrophobic interactions from the benzene rings of F48, F141, and the imidazole ring of H77, forming a three-layered sandwich with the guanine in the middle. All of these stabilizing interactions are in accordance with the experimental observations.[9,10] The Zn-bound water is positioned at 2.877 Å (O_w−C2) from the C2 of guanine, making it inaccessible for the direct nucleophilic attack, while the proton ($H1_w$) is oriented towards one of the carboxylate arms of E79 at a distance of 1.774 Å ($H1_w$-OE2) facilitating the simultaneous proton transfer. In the following section, a detailed mechanistic aspect of the deamination of guanine-bound GD has been discussed using the ONIOM approach.

Theoretical Investigation of the Reaction between Guanine and GD. On the basis of the literature available for zinc-assisted deaminases and the findings from the previous experimental study by Anand and co-workers on the substrate specificity of guanine deaminase from *Nitrosomonas europaea*, we have proposed a mechanism for the deamination of guanine, which has been depicted in Scheme 1.[20,49−51] The potential energy profile derived from the 2-layered ONIOM calculations based on Scheme 1 has been shown in Figure 3.

Activation of Zn-Bound Water. The foremost step in the deamination pathway is the activation of Zn-bound water by transferring one of the protons ($H1_w$) to the nearby carboxylate group of E79, leading to the formation of nucleophilic Zn-bound hydroxide ion (*int1*). The neighboring E79 residue has been proposed to be present in all deaminases and known to involve as a proton transporter in the previous studies.[9,10] The protonated E79/Zn-bound hydroxide (*int1*) species was found to lie at 45.8 kJ/mol higher than the initial deprotonated E79/Zn-bound water (*r*) complex. The natural charges on the Zn metal and O_w in *r* and *int1* are found to be 0.768/−0.876 and 0.783/−0.903, respectively, indicating the development of stronger negative charges on the Zn-bound hydroxyl center in *int1* (Table S2). This fact is also reflected by the shortening of the Zn−O_{wat} bond length to 1.916 Å from 2.103 Å in *r* (Figure S2A and Table S3). In *int1*, the carboxyl proton of $OE2_{E79}$ is oriented toward the N3 atom of guanine with an OE2−$H1_w$ distance of 1.032 Å with the corresponding heavy atom being hydrogen-bonded to $H1_w$ at 1.683 Å, which stabilizes the proton in $OE2_{E79}$. The other interactions between guanine and the enzyme remain intact.

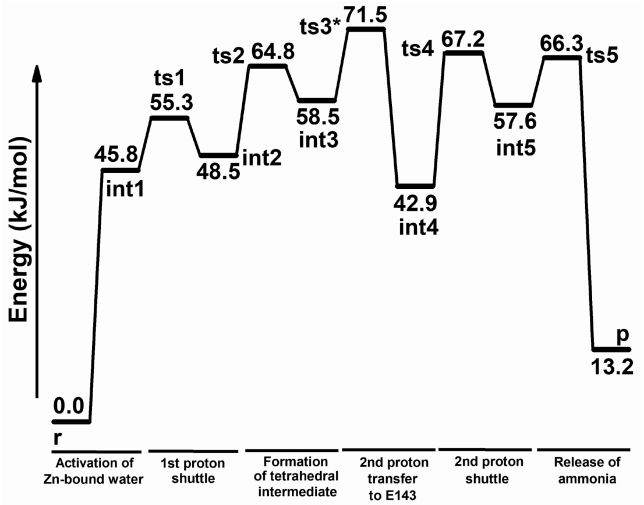

Figure 3. ONIOM (B3LYP-D2/Def2TZVP: AMBER) computed potential energy surface for the C2 deamination of guanine. Energies are in kJ/mol.

Formation of a Tetrahedral Intermediate. In the next step, the protonated arm of E79 shuttles its proton to the N3 atom of guanine resulting in the formation of *int2*, which is 64.8 kJ/mol uphill from *int1* (Figure 3). The energy barrier associated with this proton transfer transition state, *ts1*, is 55.3 kJ/mol. In *ts1*, the limiting values of newly forming N···H and the disrupting O···H bonds are found to be 1.310 and 1.205 Å, respectively (Figure 4A and Table S3). The N−H bond is completely formed in *int2* (1.048 Å) and maintained the hydrogen-bonding interaction with $OE2_{E79}$ (1.732 Å) (Figure S2B). The estimated natural charges from the natural bond orbital (NBO) analysis on the N3/C2 couple in *r* are −0.454/0.522, which after the first proton transfer in *int1* has changed to −0.624/0.730 and in *int2* to −0.662/0.752, indicating that this proton transfer step is very crucial for the reaction to proceed spontaneously because the proton on N3 makes the C2 carbon of guanine more electrophilic, and prone toward the nucleophilic attack by the newly formed Zn-bound hydroxyl group (Table S2). The intrinsic energy barrier for this hydroxyl attack is estimated to be 64.8 kJ/mol (*ts2*), leading to the formation of a tetrahedral intermediate, *int3*. In *ts2*, the critical values of 2.034 and 1.789 Å for Zn···O_{wat} and ZnO_{wat}···C2 distances are indicative of the fact that the O−C bond is starting to form without cleaving the Zn−O bond completely, indicating an early transition state (Figure 4B). In *int3*, the Zn−O_{wat} bond is further elongated to 2.110 Å, with the O_{wat}−C2 bond still coordinated to the Zn center with a distance of 1.491 Å (Figure S2C). A similar study on the cytosine deaminase (CDA) from *E. coli* by Raushel and co-workers suggested that, in the next step, the tetrahedral intermediate collapses after the deprotonation of the Zn−$O_{wat}H1_w$ group and simultaneous transfer of the proton to the amine is taking place. They suggested that the neighboring D313 assists this proton transfer.[25] In the present study, E143, which is in the substrate's vicinity, abstracts the proton from the activated hydroxide and carries it to the amine group of guanine. The consecutive intermediate (*int4*) with the protonated E143 arm is stabilized by 15.6 kJ/mol from *int3*. The second deprotonation transition state, *ts3*, is 71.5 kJ/mol from the reactant. The deprotonation is associated with the amino group of the tetrahedral intermediate moving away from the E143 residue to make room for the OE1 to abstract the Zn-bound

https://doi.org/10.1021/acs.jpcb.1c06127
J. Phys. Chem. B 2021, 125, 8814−8826

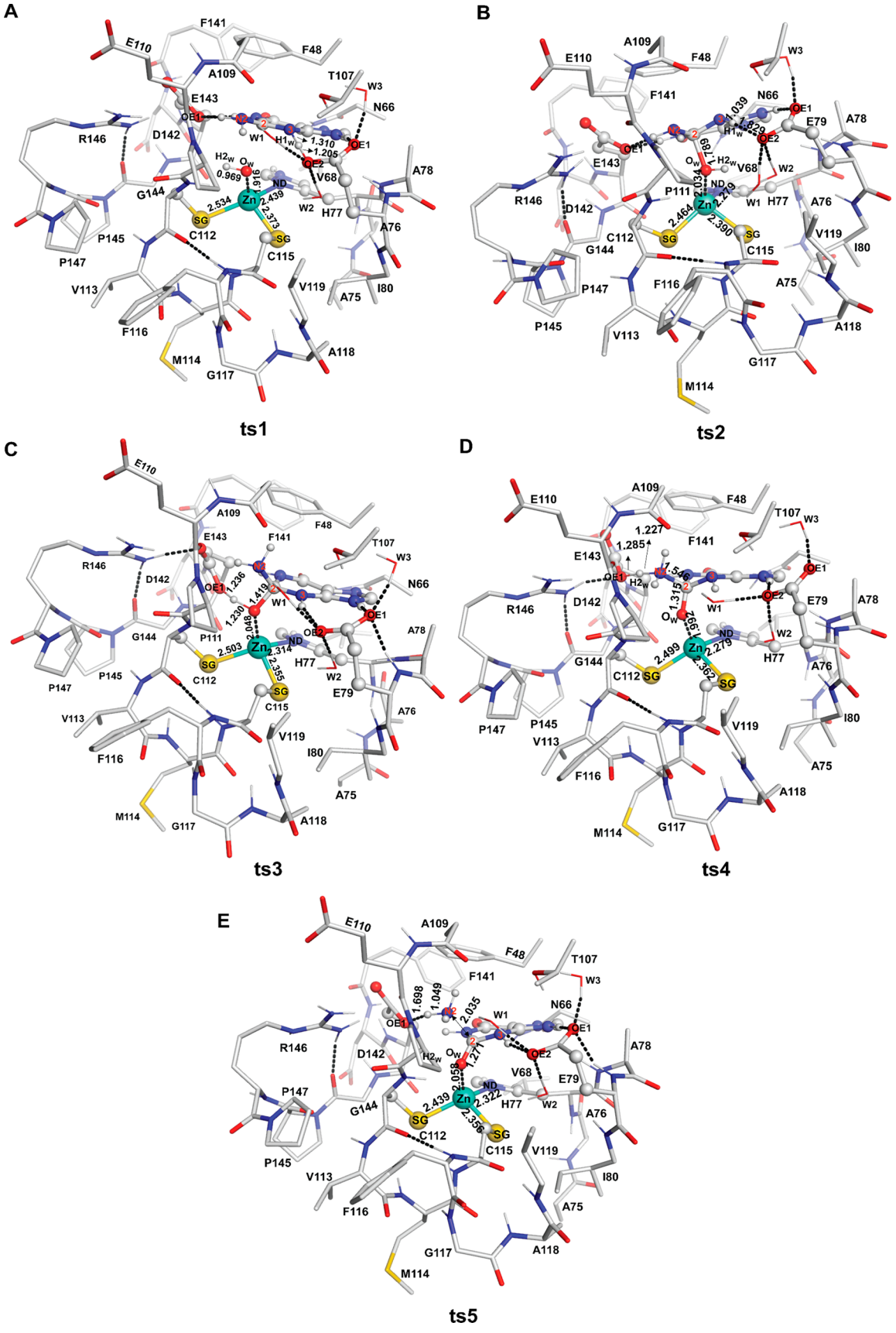

Figure 4. ONIOM (B3LYP-D2/[Lanl2DZ(Zn);6-31G*(others): AMBER) optimized structures of (A) ts1, (B) ts2, (C) ts3, (D) ts4, and (E) ts5. Bond distances are depicted in Ångström (Å) units. Zinc, sulfur, oxygen, nitrogen, carbon, and hydrogen atoms are depicted in green, yellow, red, blue, gray, and white colors, respectively.

https://doi.org/10.1021/acs.jpcb.1c06127
J. Phys. Chem. B 2021, 125, 8814−8826

hydroxyl proton. As soon as the proton is transferred, the carboxylate arm is getting stabilized by the hydrogen-bonding interaction with the amine group again. The relaxed potential energy surface scan along the $ZnO_{wat}-H1_w$ bond is associated with the constant increase in the energy during the process until the proton is transferred completely. The transition state is located at the $ZnO_{wat}-H2_w$ distance of 1.23 Å (Figure 4C). The exothermicity of the *int4* indicates that, after the proton transfer, reorientation of E143 takes place to achieve the global minima where the carboxylate proton and the amine remained hydrogen-bonded. In *int4*, the $Zn-O_{wat}$ and $ZnO_{wat}\cdots C2$ distances are shortened to 1.980 and 1.326 Å (Figure S2D), indicating the complete transfer of hydroxyl hydrogen leaving the oxo group, which acts as a bridge between the guanine and the enzyme.

Experimental results have shown that mutation of these two negatively charged amino acid residues, E79 and E143, to alanine entirely terminates the reactivity.[9,10] The ONIOM calculations also validate this fact. Both E79 and E143 residues play a crucial role in facilitating the reaction; E79 shuttles the first proton from the metal-bound water to the N3 center of guanine which helps in lowering the transition barrier for the hydroxyl attack, and E143 functions to deliver the second proton to the $-NH_2$ center, facilitating the release of ammonia. Furthermore, to assert if E143 is indeed involved, another possibility was calculated where a direct transfer of the second proton from the Zn-bound hydroxide to the amine nitrogen of the substrate was considered. The energy barrier associated with this pathway was estimated to be 145.1 kJ/mol for guanine, which is significantly larger than the path computed where the E143 residue aids proton transfer, eliminating the possibility of this pathway.

Formation of Products. In the last step, the transfer of the E143 proton to the NH_2 group of guanine takes place, forming a zwitterionic intermediate (*int5*), which simultaneously releases ammonia and ends up with xanthine as the final product (Scheme 1). In the second proton shuttle (*ts4*) step, the $OE1_{E143}\cdots H$ and $N2\cdots H$ distances are 1.285 and 1.227 Å (Figure 4D). In zwitterionic *int5*, the proton is fully transferred to the amine (N2−H = 1.109 Å) and remains hydrogen-bonded to $OE1_{E143}$(1.495 Å) (Figure S2E). In *int5*, NH3 is loosely bound to C2 (1.582 Å) and requires 66.3 kJ/mol energy to cleave the C2−N2 bond completely. The limiting value of the C2−N2 bond in *ts5* is estimated to be 2.035 Å, while those of $C2-O_w$ and $Zn-O_w$ are 1.271 and 2.058 Å (Figure 4E). The final product is significantly exothermic by 44.4 kJ/mol from *int5*, offering a strong driving force for converting ammonia and xanthine (Figure 3). After the release of ammonia, xanthine is still loosely held to the Zn ion, having a $Zn-O_{wat}$ distance of 2.173 Å (Figure S2F), which is simultaneously replaced by the water molecule, present in the reaction medium, reviving the enzyme system for the next cycle. The newly formed ammonia molecule is at 2.128 and 2.714 Å from the OE1 and OE2 of E143, and 2.167 Å from the newly forming carbonyl group of xanthine, indicating that the molecule is very loosely held and can be moved freely, favoring the reaction from an entropic point of view. Finally, the loosely bound xanthine can be easily removed, forming the product (xanthine + ammonia) and free GD. On the basis of these observations, it can be concluded that the overall reaction ($r \rightarrow p$) is found to be endothermic by 13.2 kJ/mol.

This scenario is unlike pyrimidine nucleobases, where a single negatively charged residue can assist the reaction. Thus, it appears that, in GDs, two negatively charged amino acids are essential for catalysis. Proper positioning of the substrate around both these residues is paramount for an effective deamination reaction. Since a previous ONIOM calculation by Yao et al. detailing the GD mechanism had been performed, we compared results obtained for NE0047.[20] As different positioning of the guanine ring in *Bacillus subtilis* GD suggested earlier, the roles of residues D114 and E55 (E143 and E79 in NE0047, respectively) were reversed (Figure 1D). In the corrected orientation as determined by X-ray crystallography by our group (PDB entry 4HRQ), it is easy to comprehend that the transfer of the proton from the Zn-bound water to the N3 nitrogen atom of guanine for the subsequent formation of the tetrahedral intermediate is mediated via E55 rather than D114 as proposed earlier (Figure 1D). Residue D114 plays the role of anchoring the NH_2 group to be deaminated and assists in the shuttle of the second proton from the Zn hydroxide to the amino group. Thus, the mechanism proposed in this work provides a comprehensive and complete picture of the reaction coordinate and can be generalized to other GDs (Scheme 1). The differences observed in the two calculations highlight the importance of the availability of crystal structures in the complex with substrate and substrate analogues for accurate prediction of the reaction mechanism.

Active-Site Model Calculations for Ammeline. In this section, we have studied the reactivity of GDs toward ammeline, which is, according to the experiment, the only competent substrate to be deaminated by NE0047. Interestingly, it is observed that NE0047 can deaminate ammeline while it is unable to do so toward its structurally similar substrate cytosine.[9,10] These facts fascinated us, compelling us to explore the detailed mechanistic insight, energetics, and, most importantly, the effect of the secondary coordination sphere on the catalytic activity of ammeline-bound GD. Utilizing the thorough mechanistic understanding developed from the above quantum mechanics/molecular mechanics (QM/MM) study on the reaction between guanine and GD, in this section, we have employed the QM-only method for further calculations. While the ONIOM approach considers the reaction center along with a large portion of the protein around it as the active region, the QM-only method deals with relatively simple models that generally contain all the atoms participating in the enzymatic reaction and the surrounding amino acid residues. These aid the substrate binding and stabilization, maintaining its configuration, and influence the system by short- and long-range electrostatic interactions. These QM calculations are expensive compared to the MM method, limiting the number of atoms taken as the QM part. Therefore, the choice of a suitable molecular model which contains all the structural components that directly or indirectly influence the course of the reaction, the accurate quantum chemical methodology, the explicit water molecules, and the dielectric constant of the medium is paramount. In the present study, we have considered all of these factors to propose a suitable cluster model to study ammeline deamination kinetics.[37] We have designed three active-site cluster models containing 82, 118, and 124 atoms (model-1, model-2, and model-3, respectively, Figure 2) based on the X-ray crystal structure of ammeline-bound GD (PDB: 4LCO).[9] The model-1 is the simplest one, which comprises the groups which are directly involved in the bond-making and bond-breaking processes in the reaction, the zinc metal with its first-coordination-sphere ligands (H77, C112, C115, and one Zn-bound water), and E79, D142, and E143 from the second-

https://doi.org/10.1021/acs.jpcb.1c06127
J. Phys. Chem. B 2021, 125, 8814−8826

coordination shell (Figure 2B). Model-2 and model-3 are further modified by including the effect of F48, N66 residues from the surrounding secondary coordination sphere (Figure 2C). In model-3, there are two crystallographic water molecules near the active site. These two water molecules are found to be hydrogen-bonded with the surrounding amino acid residues (Figure 2D). All residues in these models were truncated either at the α- or β-carbon atoms and subsequently saturated by hydrogen atoms. During the geometry optimizations, in all models, the tertiary carbon atoms of all residues were kept frozen to their crystallographic positions to mimic the steric effect imposed by the protein environment and to avoid unrealistic expansion of the active site during optimizations. This procedure is successfully adopted by the previous studies on metalloenzymes.[11,12,18−20] The electrostatic effect, which is generally introduced by the surrounding protein, has been incorporated on the QM model by a homogeneous polarizable continuum medium with a dielectric constant of 4.0.[16] The DFT computed potential energy diagram for the C2 deamination of ammeline is shown in Figure 5.

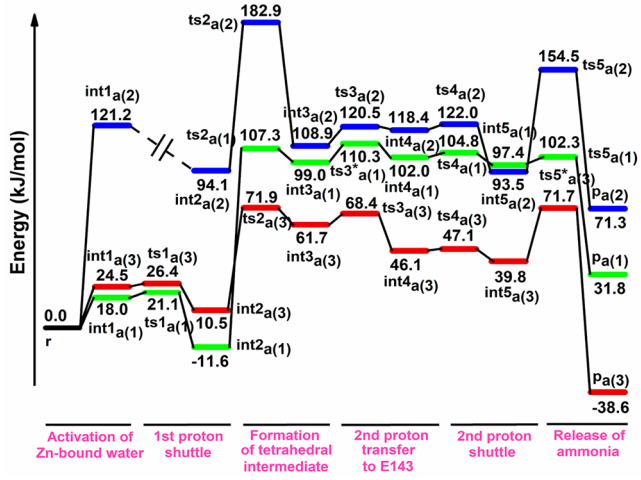

Figure 5. DFT computed potential energy surface for the C2 deamination of ammeline. Energies are in kJ/mol. The green, blue, and red lines are corresponding to model-1, model-2, and model-3, respectively.

In the high-resolution crystal structure of ammeline-bound GD (PDB: 4LCO), the Zn−O_w distance is 1.948 Å which is in good agreement with the Zn−O_w distances in the DFT optimized structure of model-1 and model-3 reactant complexes, 2.125, and 2.128 Å, respectively. The Zn−O_w bond length in model-2 is slightly higher (2.226 Å) than in the other two models (Figure 2). The other bonding parameters around the tetrahedral Zn center in the original crystal structure and all models have been tabulated in Table S4. These Zn−O_w distances in different models are directly related to the calculated natural charges on the Zn centers in those species, which are 0.815, 0.784, and 0.850 in model-1, model-2, and model-3, respectively (Tables S5−S7). A larger charge on the Zn ion leads to lower Zn−O_w distance, which increases the tendency to form Zn-bound hydroxide ($int1_a$). This fact is evident in the formation of $int1_{a(2)}$, being endothermic by 121.2 kJ/mol, while $int1_{a(1)}$ and $int1_{a(3)}$ are lying at 18.0 and 24.5 kJ/mol from the respective reactant complexes (r_a) (Figure 5). From the energy decomposition analysis (EDA), we found the destabilization due to steric factor is minimal for $int1_{a(1)}$. In contrast, E_{steric} in $int1_{a(2)}$ and $int1_{a(3)}$ is 83.8 and 69.7 kJ/mol higher than that in $int1_{a(1)}$, explaining the high endothermicity of $int1_{a(2)}$ resulting from steric crowding due to the presence of F48 and N66 residues. This steric crowding is by some means nullified by the stabilizing interaction energy and hydrogen-bonding interactions resulting from the two crystallographic water molecules in $int1_{a(3)}$, ensuing in an overall stabilization. In $int1_a$, the Zn−O_w distances are 1.970, 1.984, and 1.988 Å indicating the complete formation of the Zn hydroxyl moiety when the $H1_w$ proton has already been transferred to $OE2_{E79}$ and remains in a perfect orientation for the transfer to N3 of ammeline (N3−$H1_w$ and O_{E79}−$H1_w$ distances are 1.589 and 1.055 Å; 1.549 and 1.073 Å; 1.583 and 1.071 Å in model-1, model-2, and model-3, respectively, Figures S3A, S5A, and S7A). All bonding parameters for the stationary points involved in the reaction pathway of model-1, model-2, and model-3 are shown in Figures S3−S7 and tabulated in Tables S8−S10. The schematic diagram for the ammeline deamination reaction is depicted in Scheme S1.

In a sequential step, the proton from the E79 is transported to the N3 atom of ammeline through $ts1_a$, leading to $int2_a$ (Figures S3C, S5B, and S7B, respectively, for model-1 to model-3). The energy barrier associated with this step is 3.1 and 1.9 kJ/mol for model-1 and model-3, respectively, and this step is found to be barrierless for model-2. These transition barriers ($ts1_a$) are directly proportional to the N3−$H1_w$/O_{E79}−$H1_w$ ratio (1.50, 1.44, and 1.47, respectively, for model-1, model-2, and model-3) in $int1_a$, indicating that the O−H proton has already started to move toward N3 in $int1_{a(2)}$, making the transfer barrierless. The E_{steric} values for $ts1_{a(1)}$ and $ts1_{a(3)}$ are found to be 52.3 and 77.7 kJ/mol, which are higher than the computed energy barriers for the respective steps, indicating that the stabilizing interaction energy (E_{int}) is also playing an important role (E_{int} values for $ts1_{a(1)}$ and $ts1_{a(3)}$ are −403.8 and −391.7 kJ/mol) to compensate for the steric destabilization. Moreover, in contrast to $int1_a$, the surrounding F48 and N66 residues lower the barrier for $ts1_{a(3)}$. The potential energy surface scan along with the O_{E79}−$H1_w$ bond from 1.12 to 1.24 Å in model-2 is shown in Figure S8, showing a continuous decline in the energy with an increase in the O−H bond length suggesting the process as barrierless. In $ts1_a$, the limiting N3−$H1_w$ and O_{E79}−$H1_w$ bond distances are estimated to be 1.397 and 1.150 Å, and 1.459 and 1.125 Å, in model-1 and model-3, respectively, indicating a late transition state for model-1 and an early one for model-3 (Figures S3B and 6A and Tables S8 and S10). The formation of $int2_a$ is 11.6 kJ/mol exothermic for model-1, while the values for model-2 and model-3 are 94.1 and 10.5 kJ/mol endothermic from r_a. The steric destabilization in $int2_{a(3)}$ is 9.6 kJ/mol higher than that in model-2, leading to the exothermicity of $int2_{a(3)}$ being lower by 11.1 kJ/mol than $int2_{a(2)}$. A similar trend is followed for $int2_a$, where F48 and N66 residues are causing destabilization, with the E_{steric} for $int2_{a(1)}$ is 301.9 kJ/mol less than that of $int2_{a(2)}$. This fact can be directly correlated to the energy gap of 105.7 kJ/mol between the two.

The next step is the ZnO_{wat}−C bond formation via $ts2_a$, lying at 107.3, 182.9, and 71.9 kJ/mol from the respective reactants for model-1 to model-3. A late transition state has been found for the lowest energy $ts2_{a(3)}$, with the limiting ZnO_{wat}···C and Zn−O_w distances of 2.203 and 1.978 Å, respectively (Figure 6B), indicating that the C2−O_w bond is already formed in $ts2_{a(3)}$. However, these bonding parameters in $ts2_{a(1)}$ and $ts2_{a(2)}$ are estimated to be 1.902, 2.011 Å, and 2.182, 1.983 Å (Figures S3D and S5C). The extremely high energy barrier for the

https://doi.org/10.1021/acs.jpcb.1c06127
J. Phys. Chem. B 2021, 125, 8814−8826

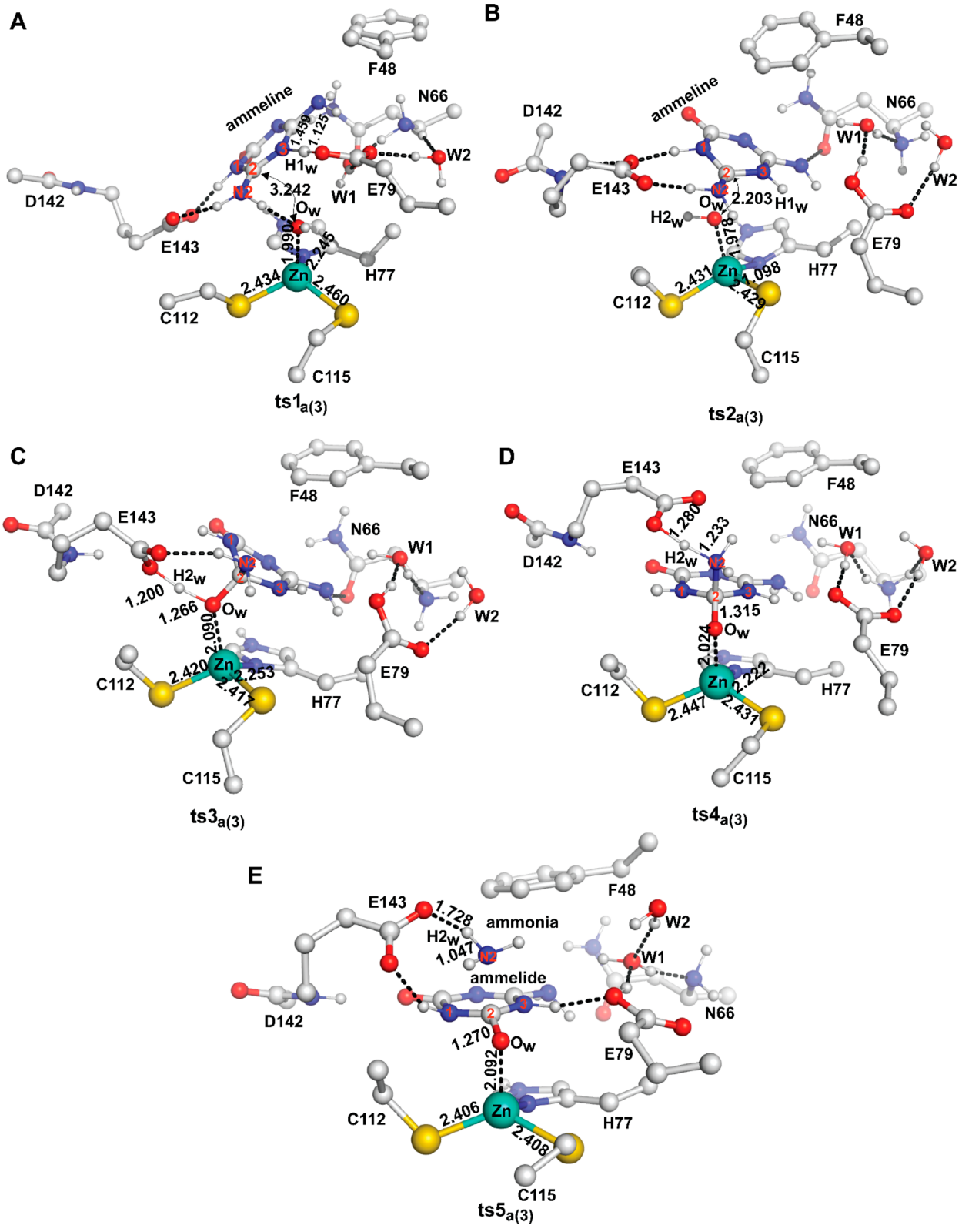

Figure 6. DFT optimized structures of (A) $ts1_{a(3)}$, (B) $ts2_{a(3)}$, (C) $ts3_{a(3)}$, (D) $ts4_{a(3)}$, and (E) $tsS_{a(3)}$. Bond distances are depicted in Ångström (Å) units. Zinc, sulfur, oxygen, nitrogen, carbon, and hydrogen atoms are depicted in green, yellow, red, blue, gray, and white, respectively.

nucleophilic attack associated with model-1 and model-2 directly eliminates these two models from further consideration. However, we have calculated the next steps in the reaction sequence related to these two models to investigate how the energetics differ due to the variation in the secondary coordination sphere. The nucleophilic attack generates $int3_{a(3)}$, stabilized by 10.2 kJ/mol compared to $ts2_{a(3)}$. For model-1 and model-2, these species lie at 99.0 and 108.9 kJ/mol in the PES. In the newly formed species ($int3_a$), the O_{wat}−C bond is found to be 1.462 Å (Figure S7C), where the second hydrogen atom in

https://doi.org/10.1021/acs.jpcb.1c06127
J. Phys. Chem. B 2021, 125, 8814−8826

O_{wat} is found to be in a proper orientation for the abstraction by E143 being hydrogen-bonded to it and, eventually, giving up the proton forming $int4_a$. The energy barrier associated with the second proton transfer ($ts3_{a(3)}$, Figure 6C) is estimated to be 68.4 kJ/mol from the reactant. The formation of $int4_{a(3)}$ is further stabilized by 15.6 kJ/mol compared to that of $int3_{a(3)}$. The O_{wat}−C bond is fully formed in $int4_{a(3)}$ (1.321 Å, Figure S7D). For model-1 and model-3, the bonding parameters for $int3_a$ and $int4_a$ are shown in Figures S3E, S4A, S5D, and S5F.

In the following step, the amino group is protonated ($int5_a$) by the proton donation from the carboxyl arm of the neighboring E143 residue followed by the C2−N2 bond cleavage leading to the formation of ammelide along with free ammonia. The second proton transfer to amine is less energy demanding, 47.1 kJ/mol ($ts4_{a(3)}$), than the other transition states involved in the pathway. The O_{E143}−$H2_w$ and N2−$H2_w$ bond lengths in $ts4_{a(3)}$ associated with the breaking and making process are 1.280 and 1.233 Å, Figure 6D (Figures S4B and S6A for model-1 and model-2). Similar to the previous cases, we found this energy barrier for model-1 and model-2 to be very high, 57.7 and 74.9 kJ/mol more elevated than that of model-3 (Figure 5). This energy elevation can be directly correlated to the steric reason; E_{steric} is estimated to be 215.7, 29.9, and −4.1 kJ/mol, respectively. From the above E_{steric} values, we can conclude that, in the case of *ts4a*, the introduction of N66 and F48 residues in model-2 lowers the steric strain significantly compared to that of model-1. Further inclusion of two crystal water molecules in model-3 results in more stabilization to $ts4_{a(3)}$. This contrasts with $int1_a$ and $int2_a$, where the introduction of F48 and N66 residues increases the steric strain. The $int5_a$ is lying at 7.3, 28.5, and 7.3 kJ/mol downhill compared to their respective transition states for the three models. In *int5*, the second proton is completely transferred to the amine and remained hydrogen-bonded to E143. The zwitterionic NH_3 moiety is loosely held to the C2 carbon (1.610 Å, 1.568 Å, 1.539 Å, respectively, for model-1 to model-3, Figures S4C, S6B, and S7E) to be detached in the next step.

The energy requirement for this ammonia release is 102.3 kJ/mol ($ts5_{a(1)}$) and 154.5 kJ/mol ($ts5_{a(2)}$) for model-1 and model-2, respectively. Although $ts5_{a(1)}$ and $ts5_{a(2)}$ are fully optimized (Figures S4D and S6C), all of our attempts to get the $ts5_{a(3)}$ transition state have failed as it converges to $int4_{a(3)}$ every time. To affirm the barrier associated with the ammonia release step for model 3, a potential energy surface scan along the C2−N2 distance from 1.5 to 2.3 Å has been performed and finds the maximum energy associated with the C2−N2 distance of 2.0 Å with the barrier of 71.7 kJ/mol (Figure 6E and Figure S9). Similar to the previous transition states, in $ts5_a$, F48, N66, and two crystallographic waters help in lowering the steric strain in model-1 (E_{steric} = 221.7 kJ/mol) and model-3 (E_{steric} = 168.9 kJ/mol) than in model-2 (E_{steric} = 398.9 kJ/mol). Therefore, from the above discussion, we can conclude that the F48 and N66 groups in the secondary coordination sphere destabilize the $int1_a$ and $int2_a$ while these groups are important for stabilizing the transition states. Here the crystallographic water molecules in model-3 come to play, forming a stable hydrogen-bonding interactions facilitating the formation of intermediates and the transition states during the reaction. Therefore, model-3 is the best model for the mechanistic study of ammeline deamination. For model-3, the ammelide-bound enzyme complex, $p_{a(3)}$, is 110.3 kJ/mol downhill from the reactant, making the overall ammeline deamination reaction exothermic by 38.6 kJ/mol from *r*. In the $p_{a(3)}$, the Zn−O_{wat} and the newly formed C═O_w bonds in ammelide are found to be 2.208 and 1.246 Å, and the free ammonia molecule remains hydrogen-bonded to the neighboring E143 (1.976 Å) and a crystallographic water molecule (1.799 Å) (Figure S7F). The bonding parameters for model-1 and model-2 have been shown in Figures S3−S6.

The essential role of various secondary coordination sphere residues as a proton shuttle has been established in previous studies. Himo and co-workers have explored the reactivity of cytosine deaminase and suggested that the initial deprotonation of Zn-bound water is assisted by Glu217 followed by the protonation of the ring nitrogen and subsequent transfer of the second proton to the substrate amine group via Asp313, supporting our observations.[49−52] Zhang et al. have reported a similar mechanism for the hydrolytic deamination mechanism by the yeast cytosine deaminase (yCD) employing QM/MM methodology.[19] Computational findings from the work of Yan and co-workers on the deamination reaction catalyzed by *Bacillus subtilis* guanine deaminase also support the involvement of various groups in the secondary coordination sphere during the proton shuttle.[20] The mechanistic details and the energetics obtained from these studies are in line with our observation, providing confidence in the adopted methodology, the model structures, and the deamination mechanism in the present study.

For enzymatic systems, it has been proven that the overall rate does not depend on the single transition state or the intermediate but is regulated by several microstates; i.e., more than one intermediate and the transition states dictate the catalytic reactivity. In the above pathway, none of the states is too high in energy and can be easily overcome at the experimental reaction condition, indicating that the proposed mechanism defines well the deamination reaction.

Evolutionary Conservation of Mechanism in GDs. The detailed study of the mechanism of the CDA superfamily GD prompted the question of whether a similar mechanism also operates in eukaryotic AHS, GDs especially, as both catalyze the metal-dependent reaction and exhibit moonlighting activity toward ammeline.[9,10,15] To investigate this possibility, attempts to superimpose both GDs yielded nonoptimal results owing to their completely diverse folds. However, a closer examination revealed a pattern that showed several of the active-site features of both the GDs are similar though differentially located. The position of the metal ion with respect to guanine appeared to be inverted in both structures. The negatively charged residues required as proton shuttles (E243 and D330 in hGD; E79 and E143 in NE0047) are present in both the enzymes. Even the anchoring of the O6 oxygen atom of guanine is via amino acids containing the same headgroup (N66 in NE0047 and Q87 in hGD) (Figure S10A,B). Additionally, the hydrophobic residues stabilize the purine ring in both enzymes, albeit from different directions. While the CDA superfamily GDs require the closure of the C-terminal loop for efficient catalysis, AHS GD has an active site that is more buried, and shielding is provided by a conserved arginine residue. Therefore, we can conclude that both the AHS and the CDA superfamily GDs catalyze deamination reactions using a similar set of residues and hence utilize the same catalytic mechanism for the efficient release of ammonia. It is noteworthy to stress that both of these enzymes exhibit a similar substrate selectivity profile and can catalyze the two structurally nonhomologous substrates, guanine, and ammeline. This fact cannot be a mere coincidence, and the current analysis highlights the subtle evolutionary link in the seemingly diverse system that governs the underlining catalytic mechanism.[9,10,15] However, since the location and the

https://doi.org/10.1021/acs.jpcb.1c06127
J. Phys. Chem. B 2021, 125, 8814−8826

architecture of both of these active sites are diverse, and even the shielding residues are not analogous, efforts to make selective inhibitors of bacterial GDs can be logically undertaken. Moreover, GDs require two proton shuttles instead of one; hence, inhibitors targeting the second proton shuttle (E143 in NE0047) can be a specific target for drug design. These efforts may purport new directions in drug discovery.

CONCLUSIONS

In the current work, we have explored mechanistic details of the C2 deamination of guanine and ammeline by bacterial GDs using the 2-layered ONIOM method (QM:MM) and the small models using the density functional theory (DFT) method. The ONIOM calculations on the guanine-bound GD provide an excellent description of the mechanism and agree well with the experiments on many counts. The QM-only (DFT) results with the smallest model (active site only) of the ammeline-bound GD are not satisfactory, and larger models, including F48 and N66 and two crystallographic water molecules, surprisingly turned things around. These crystal waters involved in the hydrogen-bonding interactions with the active site and the neighboring amino acid residues make a hydrogen-bonding channel and stabilize both the transition states and intermediates during the reaction. Therefore, the model having the optimum balance of the stabilizing and destabilizing factors on the stationary points is found to be the best cluster model among those studied.

Mechanistically, results clearly show that there is a requirement of two proton shuttles in purine deaminating enzymes. While the E79 residue, which is commonly present in all deaminases, delivers the first proton from Zn-bound water to the N3 atom of the substrate, the E143 helps in the transportation of the second proton to the amine group, facilitating the release of ammonia. In the absence of E143, the second proton shuttle for guanine is highly energy-demanding, eliminating the possibility of direct proton transfer to the amine. To this end, the catalytic mechanism proposed here is generic, and the knowledge generated here can be applied to both the eukaryotic and prokaryotic systems toward developing selective drug therapies.

ASSOCIATED CONTENT

Supporting Information

The Supporting Information is available free of charge at https://pubs.acs.org/doi/10.1021/acs.jpcb.1c06127.

Scheme S1, Figures S1−S9, and Tables S1−S10, depicting mechanisms, structures, and additional results (PDF)

AUTHOR INFORMATION

Corresponding Authors

Ruchi Anand − *Department of Chemistry, Indian Institute of Technology—Bombay, Mumbai 400076, India;* orcid.org/0000-0002-2045-3758; Email: ruchi@chem.iitb.ac.in

Gopalan Rajaraman − *Department of Chemistry, Indian Institute of Technology—Bombay, Mumbai 400076, India;* orcid.org/0000-0001-6133-3026; Email: rajaraman@chem.iitb.ac.in

Authors

Asmita Sen − *Department of Chemistry, Indian Institute of Technology—Bombay, Mumbai 400076, India*

Vandana Gaded − *Department of Chemistry, Indian Institute of Technology—Bombay, Mumbai 400076, India*

Prabha Jayapal − *Department of Chemistry, Indian Institute of Technology—Bombay, Mumbai 400076, India*

Complete contact information is available at: https://pubs.acs.org/10.1021/acs.jpcb.1c06127

Author Contributions

A.S. contributed to calculations, data analysis, and manuscript writing. V.G. and P.J. contributed to project designing and manuscript writing. R.A. and G.R. contributed to overall supervision of the project.

Notes

The authors declare no competing financial interest.

ACKNOWLEDGMENTS

This work was funded by DST, Government of India (Grants EMR/2015/002121 and DST/TM/WTI/2K16/252). G.R. would like to thank DST/SERB for funding (CRG/2018/000430; DST/SJF/CSA-03/2018-10; SB/SJF/2019-20/12), and A.S. thanks CSIR for the SRF fellowship.

REFERENCES

(1) Lane, A. N.; Fan, T. W. Regulation of mammalian nucleotide metabolism and biosynthesis. *Nucleic Acids Res.* **2015**, *43* (4), 2466−2485.

(2) Barsotti, C.; Tozzi, M. G.; Ipata, P. L. Purine and pyrimidine salvage in whole rat brain: Utilization of ATP-derived ribose-1-phosphate and 5-phosphoribosyl-1-pyrophosphate generated in experiments with dialyzed cell-free extracts. *J. Biol. Chem.* **2002**, *277* (12), 9865−9869.

(3) Moffatt, B. A.; Ashihara, H. Purine and pyrimidine nucleotide synthesis and metabolism. *Arabidopsis Book/American Society of Plant Biologists* **2002**, *1*, e0018.

(4) Iyer, L. M.; Zhang, D.; Rogozin, I. B.; Aravind, L. Evolution of the deaminase fold and multiple origins of eukaryotic editing and mutagenic nucleic acid deaminases from bacterial toxin systems. *Nucleic Acids Res.* **2011**, *39* (22), 9473−9497.

(5) Ko, T. P.; Lin, J. J.; Hu, C. Y.; Hsu, Y. H.; Wang, A. H.; Liaw, S. H. Crystal structure of yeast cytosine deaminase. Insights into enzyme mechanism and evolution. *J. Biol. Chem.* **2003**, *278* (21), 19111−7.

(6) Liaw, S. H.; Chang, Y. J.; Lai, C. T.; Chang, H. C.; Chang, G. G. Crystal structure of Bacillus subtilis guanine deaminase: the first domain-swapped structure in the cytidine deaminase superfamily. *J. Biol. Chem.* **2004**, *279* (34), 35479−85.

(7) Gaded, V.; Anand, R. Nucleobase deaminases: a potential enzyme system for new therapies. *RSC Adv.* **2018**, *8* (42), 23567−23577.

(8) Pang, B.; McFaline, J. L.; Burgis, N. E.; Dong, M.; Taghizadeh, K.; Sullivan, M. R.; Elmquist, C. E.; Cunningham, R. P.; Dedon, P. C. Defects in purine nucleotide metabolism lead to substantial incorporation of xanthine and hypoxanthine into DNA and RNA. *Proc. Natl. Acad. Sci. U. S. A.* **2012**, *109* (7), 2319.

(9) Bitra, A.; Biswas, A.; Anand, R. Structural basis of the substrate specificity of cytidine deaminase superfamily Guanine deaminase. *Biochemistry* **2013**, *52* (45), 8106−14.

(10) Bitra, A.; Hussain, B.; Tanwar, A. S.; Anand, R. Identification of Function and Mechanistic Insights of Guanine Deaminase from Nitrosomonas europaea: Role of the C-Terminal Loop in Catalysis. *Biochemistry* **2013**, *52* (20), 3512−3522.

(11) Gaded, V.; Anand, R. Selective Deamination of Mutagens by a Mycobacterial Enzyme. *J. Am. Chem. Soc.* **2017**, *139* (31), 10762−10768.

(12) Nygaard, P.; Bested, S. M.; Andersen, K. A.; Saxild, H. H. Bacillus subtilis guanine deaminase is encoded by the yknA gene and is induced during growth with purines as the nitrogen source. *Microbiology* **2000**, *146* (12), 3061−9.

(13) Fernandez, J. R.; Sweet, E. S.; Welsh, W. J.; Firestein, B. L. Identification of small molecule compounds with higher binding affinity

to guanine deaminase (cypin) than guanine. *Bioorg. Med. Chem.* **2010**, *18* (18), 6748−55.
(14) Yuan, G.; Bin, J. C.; McKay, D. J.; Snyder, F. F. Cloning and characterization of human guanine deaminase. Purification and partial amino acid sequence of the mouse protein. *J. Biol. Chem.* **1999**, *274* (12), 8175−80.
(15) Seffernick, J. L.; Dodge, A. G.; Sadowsky, M. J.; Bumpus, J. A.; Wackett, L. P. Bacterial ammeline metabolism via guanine deaminase. *J. Bacteriol.* **2010**, *192* (4), 1106−12.
(16) Sklenak, S.; Yao, L.; Cukier, R. I.; Yan, H. Catalytic mechanism of yeast cytosine deaminase: an ONIOM computational study. *J. Am. Chem. Soc.* **2004**, *126* (45), 14879−89.
(17) Yao, L.; Sklenak, S.; Yan, H.; Cukier, R. I. A molecular dynamics exploration of the catalytic mechanism of yeast cytosine deaminase. *J. Phys. Chem. B* **2005**, *109* (15), 7500−10.
(18) Yao, L.; Yan, H.; Cukier, R. I. A combined ONIOM quantum chemical-molecular dynamics study of zinc-uracil bond breaking in yeast cytosine deaminase. *J. Phys. Chem. B* **2006**, *110* (51), 26320−6.
(19) Zhang, X.; Zhao, Y.; Yan, H.; Cao, Z.; Mo, Y. Combined QM(DFT)/MM molecular dynamics simulations of the deamination of cytosine by yeast cytosine deaminase (yCD). *J. Comput. Chem.* **2016**, *37* (13), 1163−74.
(20) Yao, L.; Cukier, R. I.; Yan, H. Catalytic mechanism of guanine deaminase: an ONIOM and molecular dynamics study. *J. Phys. Chem. B* **2007**, *111* (16), 4200−10.
(21) Pronk, S.; Páll, S.; Schulz, R.; Larsson, P.; Bjelkmar, P.; Apostolov, R.; Shirts, M. R.; Smith, J. C.; Kasson, P. M.; van der Spoel, D.; et al. GROMACS 4.5: a high-throughput and highly parallel open source molecular simulation toolkit. *Bioinformatics* **2013**, *29* (7), 845−854.
(22) Sousa da Silva, A. W; Vranken, W. F ACPYPE-Antechamber python parser interface. *BMC Res. Notes* **2012**, *5* (1), 367.
(23) Schrödinger, L. *The PyMOL Molecular Graphics System*, version 1.8; November, 2015.
(24) Antony, J.; Grimme, S. Density functional theory including dispersion corrections for intermolecular interactions in a large benchmark set of biologically relevant molecules. *Phys. Chem. Chem. Phys.* **2006**, *8* (45), 5287−5293.
(25) Frisch, M. J.; Trucks, G. W.; Schlegel, H. B.; Scuseria, G. E.; Robb, M. A.; Cheeseman, J. R.; Scalmani, G.; Barone, V.; Mennucci, B.; Petersson, G. A.; et al. *Gaussian 09, Revision A.1*; Gaussian. Inc.: Wallingford, CT, 2009; Vol. *121*, pp 150−166.
(26) Gordon, J. C.; Myers, J. B.; Folta, T.; Shoja, V.; Heath, L. S.; Onufriev, A. H++: a server for estimating p K as and adding missing hydrogens to macromolecules. *Nucleic Acids Res.* **2005**, *33* (suppl_2), W368−W371.
(27) Mark, P.; Nilsson, L. Structure and dynamics of the TIP3P, SPC, and SPC/E water models at 298 K. *J. Phys. Chem. A* **2001**, *105* (43), 9954−9960.
(28) Petrova, S. S.; Solov'ev, A. D. The origin of the method of steepest descent. *Hist. Math.* **1997**, *24* (4), 361−375.
(29) Bussi, G.; Donadio, D.; Parrinello, M. Canonical sampling through velocity rescaling. *J. Chem. Phys.* **2007**, *126* (1), 014101.
(30) Bjelkmar, P.; Larsson, P.; Cuendet, M. A.; Hess, B.; Lindahl, E. Implementation of the CHARMM force field in GROMACS: analysis of protein stability effects from correction maps, virtual interaction sites, and water models. *J. Chem. Theory Comput.* **2010**, *6* (2), 459−466.
(31) Evans, D. J.; Holian, B. L. The nose-hoover thermostat. *J. Chem. Phys.* **1985**, *83* (8), 4069−4074.
(32) Hess, B.; Kutzner, C.; Van Der Spoel, D.; Lindahl, E. GROMACS 4: algorithms for highly efficient, load-balanced, and scalable molecular simulation. *J. Chem. Theory Comput.* **2008**, *4* (3), 435−447.
(33) Darden, T.; York, D.; Pedersen, L. Particle mesh Ewald: An N log (N) method for Ewald sums in large systems. *J. Chem. Phys.* **1993**, *98* (12), 10089−10092.
(34) Andersen, H. C. Rattle: A "velocity" version of the shake algorithm for molecular dynamics calculations. *J. Comput. Phys.* **1983**, *52* (1), 24−34.
(35) Svensson, M.; Humbel, S.; Froese, R. D.; Matsubara, T.; Sieber, S.; Morokuma, K. ONIOM: a multilayered integrated MO+ MM method for geometry optimizations and single point energy predictions. A test for Diels- Alder reactions and Pt (P (t-Bu) 3) 2+ H2 oxidative addition. *J. Phys. Chem.* **1996**, *100* (50), 19357−19363.
(36) Vreven, T.; Byun, K. S.; Komáromi, I.; Dapprich, S.; Montgomery Jr, J. A.; Morokuma, K.; Frisch, M. J. Combining quantum mechanics methods with molecular mechanics methods in ONIOM. *J. Chem. Theory Comput.* **2006**, *2* (3), 815−826.
(37) Ahmadi, S.; Barrios Herrera, L.; Chehelamirani, M.; Hostaš, J.; Jalife, S.; Salahub, D. R. Multiscale modeling of enzymes: QM-cluster, QM/MM, and QM/MM/MD: A tutorial review. *Int. J. Quantum Chem.* **2018**, *118* (9), No. e25558.
(38) Chung, L. W.; Sameera, W.; Ramozzi, R.; Page, A. J.; Hatanaka, M.; Petrova, G. P.; Harris, T. V.; Li, X.; Ke, Z.; Liu, F.; et al. The ONIOM method and its applications. *Chem. Rev.* **2015**, *115* (12), 5678−5796.
(39) Becke, A. D. Density-functional thermochemistry. V. Systematic optimization of exchange-correlation functionals. *J. Chem. Phys.* **1997**, *107* (20), 8554−8560.
(40) Grimme, S.; Antony, J.; Ehrlich, S.; Krieg, H. A consistent and accurate ab initio parametrization of density functional dispersion correction (DFT-D) for the 94 elements H-Pu. *J. Chem. Phys.* **2010**, *132* (15), 154104.
(41) Hehre, W. J.; Ditchfield, R.; Pople, J. A. Self—consistent molecular orbital methods. XII. Further extensions of Gaussian—type basis sets for use in molecular orbital studies of organic molecules. *J. Chem. Phys.* **1972**, *56* (5), 2257−2261.
(42) Rassolov, V. A.; Pople, J. A.; Ratner, M. A.; Windus, T. L. 6-31G* basis set for atoms K through Zn. *J. Chem. Phys.* **1998**, *109* (4), 1223−1229.
(43) Rassolov, V. A.; Ratner, M. A.; Pople, J. A.; Redfern, P. C.; Curtiss, L. A. 6-31G* basis set for third-row atoms. *J. Comput. Chem.* **2001**, *22* (9), 976−984.
(44) Frisch, M.; Frisch, M.; Trucks, G.; Schlegel, K. H.; Scuseria, G.; Robb, M. A.; Cheeseman, J.; Montgomery, J.; Vreven, T.; Kudin, K. N. *Gaussian 03, revision D.02*; Gaussian. Inc.: Wallingford, CT, 2004.
(45) Frisch, M.; Trucks, G. W.; Schlegel, H. B.; Scuseria, G. E.; Robb, M. A.; Cheeseman, J. R.; Scalmani, G.; Barone, V.; Mennucci, B.; Petersson, G. A. *Gaussian 09, Revision D.01*; Gaussian. Inc.: Wallingford, CT, 2014.
(46) Frisch, M. J.; Trucks, G. W.; Schlegel, H. B.; Scuseria, G. E.; Robb, M. A.; Cheeseman, J. R.; Scalmani, G.; Barone, V.; Petersson, G. A.; Nakatsuji, H.; et al. *Gaussian 16, Rev. B.01*; Gaussian. Inc.: Wallingford, CT, 2016.
(47) Grimme, S.; Antony, J.; Ehrlich, S.; Krieg, H. A consistent and accurate ab initio parametrization of density functional dispersion correction (DFT-D) for the 94 elements H-Pu. *J. Chem. Phys.* **2010**, *132* (15), 154104.
(48) Cossi, M.; Rega, N.; Scalmani, G.; Barone, V. Energies, structures, and electronic properties of molecules in solution with the C-PCM solvation model. *J. Comput. Chem.* **2003**, *24* (6), 669−681.
(49) Manta, B.; Raushel, F. M.; Himo, F. Reaction mechanism of zinc-dependent cytosine deaminase from Escherichia coli: A quantum-chemical study. *J. Phys. Chem. B* **2014**, *118* (21), 5644−5652.
(50) Luo, M.; Schramm, V. L. Transition State Structure of E. coli t RNA-Specific Adenosine Deaminase. *J. Am. Chem. Soc.* **2008**, *130* (8), 2649−2655.
(51) Alberto, M. E.; Leopoldini, M.; Russo, N. Can human prolidase enzyme use different metals for full catalytic activity? *Inorg. Chem.* **2011**, *50* (8), 3394−3403.
(52) Hall, R. S.; Fedorov, A. A.; Xu, C.; Fedorov, E. V.; Almo, S. C.; Raushel, F. M. Three-dimensional structure and catalytic mechanism of cytosine deaminase. *Biochemistry* **2011**, *50* (22), 5077−5085.

https://doi.org/10.1021/acs.jpcb.1c06127
J. Phys. Chem. B 2021, 125, 8814−8826